DOI: 10.13009/EUCASS2019-359

Paper number 359

Computational Analysis of Urban Air Mobility Vehicles

Patricia Ventura Diaz* and Seokkwan Yoon†
NASA Ames Research Center
Moffett Field, California, 94035, USA

Abstract

High-fidelity computational fluid dynamics simulations of multi-rotor urban air mobility vehicles have been carried out. The capacity for vertical lift, together with the great maneuverability, make multi-rotor vehicles an excellent choice for air taxi operations. The three-dimensional unsteady Navier-Stokes equations are solved on overset grids using high-order accurate schemes, dual-time stepping, and a hybrid turbulence model using NASA's code Overflow. The flow solver has been loosely coupled with a rotorcraft comprehensive analysis code. The vehicles studied consist of small to medium sized drones, and bigger vehicles for future urban air mobility applications. The concept vehicles are intended to focus and guide NASA research activities in support of aircraft development for emerging aviation markets, in particular vertical take-off and landing air taxi operations.

Nomenclature

a	Fluid speed of sound
A	Rotor disk area, πR^2
c	Local rotor blade chord length
C'	Sectional chord force
c_{tip}	Rotor blade tip chord length
C_Q	Torque coefficient, $\frac{Q}{\rho(\Omega R)^2 RA}$
C_T	Thrust coefficient, $\frac{T}{\rho(\Omega R)^2 A}$
M'	Sectional blade pitching moment
M	Mach number, $\frac{V}{a}$
M_{tip}	Mach number at the blade tip, $\frac{\Omega R}{a}$
$M^2 c_c$	Sectional chord force coefficient, $\frac{C'}{\frac{1}{2}\rho a^2 c}$
$M^2 c_m$	Sectional pitching moment coefficient, $\frac{M'}{\frac{1}{2}\rho a^2 c^2}$
$M^2 c_n$	Sectional normal force coefficient, $\frac{N'}{\frac{1}{2}\rho a^2 c}$
N'	Sectional blade normal force
r	Radial position
R	Rotor radius
Re	Reynolds number, $\frac{VL_{ref}}{\nu}$
Re_{tip}	Reynolds number at the blade tip, $\frac{\Omega R c_{tip}}{\nu}$
V_∞	Freestream velocity
y^+	Non-dimensional viscous wall spacing
α	Angle of attack, AoA
δ	Boundary layer thickness
Δ	Grid spacing
μ	Advance ratio, $\frac{V_\infty cos(\alpha)}{\Omega R}$
ν	Fluid kinematic viscosity
ρ	Fluid density
Ω	Rotor rotational speed

*Science & Technology Corporation.
†NASA Advanced Supercomputing Division.

DOI: 10.13009/EUCASS2019-359

1. Introduction

Electric multi-rotor vehicles have grown very popular over the past decade. While originally conceived for military purposes, their simplicity and affordability have made small drones, or Unmanned Aerial Vehicles (UAVs), accessible to the civil market. They are being used for photography, film recording, and also for recreational purposes, to name just a few applications. In addition, the unique ability of multi-rotor vehicles for vertical lift has great potential for human and cargo transportation in urban areas.

Figure 1: An artist impression of an urban air mobility environment, where air vehicles with a variety of missions and with or without pilots, are able to interact safely and efficiently.

NASA and a community of government, industry, and academic partners are working together on this goal, known as Urban Air Mobility (UAM). UAM is a safe and efficient air transportation system where everything from small package delivery drones to passenger-carrying air taxis operate over populated areas, from small towns to the largest cities. Figure 1 shows an artist's impression of an UAM environment, where different air vehicles move and interact safely in the airspace.

Relying on either fully electric or hybrid propulsion systems, the eVTOL (electrical Vertical Take-Off and Landing) vehicles would transport cargo or a small number of passengers from point to point in highly congested cities, avoiding ground traffic and potentially providing a greener means of transportation. Their capacity to hover and to perform VTOL, together with their great maneuverability, make multi-rotor vehicles an excellent choice for UAM aircraft.

Accurate prediction of rotorcraft performance and acoustics continues to be challenging from a computational point of view. The flows are inherently unsteady, nonlinear, and complex. The aerodynamic interactions between multiple rotors, fuselage, and lifting bodies make it even more difficult. High-fidelity Computational Fluid Dynamics (CFD) approaches offer an advantage over low- and mid-fidelity tools for this type of flow. In addition, high-fidelity simulations can provide the information needed to calibrate lower fidelity tools that could be used for design purposes.

The designs of conventional helicopters and airplanes have been well established and optimized during the twentieth century. However, the design space of eVTOL aircraft remains wide open, and exploration for improved designs continues. NASA is exploring rotorcraft designs for VTOL air taxi operations, and several concept vehicles have been developed. Ventura Diaz *et al.*[1] performed a computational study of one of these vehicles: the side-by-side urban air taxi, confirming that two overlapped intermeshing rotors are more efficient in cruise than twin separated rotors.[2]

Previous computational work on small multi-rotor vehicles by Ventura Diaz *et al.*[3–5] and Yoon *et al.*[6,7] includes studies of the aerodynamic interactions, ducted rotors, rotor placement, torque balanced coaxial octo-rotors, and the effect of wind gusts on a hovering quadrotor. Johnson *et al.*[8,9] conducted a comprehensive analysis study using multidisciplinary design, analysis, and optimization techniques, for several multi-rotor vehicles, including three concept vehicles for the UAM mission: a quadrotor, a side-by-side helicopter, and a lift+cruise VTOL vehicle.

UAM has to ensure safe, quiet, and efficient vehicles in order to be able to fly in our cities. The objective of the present work is to demonstrate a high-fidelity simulation capability to study the complex interactional aerodynamics of multi-rotor vehicles for different flight conditions and configurations, and to establish the good practice in the design of multi-rotor UAVs and multi-rotor craft for UAM.

Three different vehicles, described below, have been studied: the DJI Phantom 3, the SUI Endurance quadcopter, and the side-by-side UAM concept.

DOI: 10.13009/EUCASS2019-359

1.1 The DJI Phantom 3

The DJI Phantom 3 is an example of a classic commercial quadcopter design with a symmetric X-shaped airframe, see Figure 2. It can be used to hover above static or slow-moving objects, to record high quality videos for example. Overset grids have been generated for the DJI Phantom 3 simplified quadcopter, which consists of the X-shaped airframe and the four rotors. The effect of over- and undermounting the rotors in hover is calculated with CFD simulations. Results for an octocopter concept are shown.

Figure 2: DJI Phantom 3 quadcopter.

1.2 The SUI Endurance

The SUI Endurance is an example of a forward-flight quadcopter design with an elongated airplane-like airframe that can be used for missions in which the UAV will be operating during most of its flight envelope in forward-flight mode, see Figure 3. Thus, it is designed for faster speeds in forward flight than a regular quadcopter, and it can be used for cargo transportation or video recording of fast-moving objects. This study focuses on the performances and characteristics of the flow in forward flight for the SUI Endurance. Three configurations are studied here, in order to see the effect of over- and undermounted rotors on aerodynamic efficiency. The first configuration, the SUI standard, is the original configuration for the SUI Endurance UAV, where the four rotors are overmounted. In the second configuration, the SUI hybrid, the fore rotors are undermounted and the aft rotors are overmounted. The third configuration is the SUI undermounted, where all rotors are placed underneath the arms. The performances of the three configurations are compared in forward flight.

Figure 3: SUI Endurance quadcopter.

1.3 NASA's Side-by-side Air Taxi Concept

Urban air taxi operations, also known as UAM applications, are enabled by VTOL capability. Power and energy requirements are minimized by using low disk-loading rotors, and short range requirements permit consideration of non-traditional propulsion concepts.

NASA's side-by-side (SbS) conceptual design is a six-passenger, 200 nm range helicopter with hybrid propulsion; see Figure 4. The SbS parallel hybrid propulsion system has two turboshaft engines, plus a motor/generator and a battery. The motor is used for hover and low speed flight, and in cruise the motor is driven as a generator by the turboshaft engine to charge the battery. The rotors of the side-by-side aircraft are overlapped by 15% (wingspan is 85% of the rotor diameter) for optimum cruise performance.[1] In addition, the aircraft with overlapping rotors offers a more compact design, which is a preferred configuration in crowded urban environments. The performance of the SbS is accurately calculated by using a loose-coupling approach of the flow solve with the rotorcraft comprehensive code. The effects of rotor overlap distance on cruise efficiency are analyzed.

Figure 4: NASA's side-by-side UAM air taxi concept.

DOI: 10.13009/EUCASS2019-359

2. Numerical Approach

The flow solver used in this study is NASA's Overflow[10] CFD solver. Overflow is a finite-difference, structured overset grid, high-order accurate Navier-Stokes flow solver. NASA's Chimera Grid Tools (CGT)[11] overset grid generation software is used for generating the overset grids of rotors and complete vehicles. Body-fitted curvilinear near-body (NB) grids are generated using CGT. The computational domain is completed with the generation of Cartesian off-body (OB) grids that are automatically generated prior to grid assembly using the domain connectivity framework in Overflow-D mode. The current time-accurate approach consists of an inertial coordinate system where NB curvilinear O-grids for the rotor blades rotate through the fixed OB Cartesian grid system. Overflow is coupled in a loosely manner with the helicopter comprehensive code CAMRAD II.[12] The CFD provides high-fidelity, nonlinear aerodynamics that replace the comprehensive lifting line aerodynamic analysis from CAMRAD II. The comprehensive code performs the structural dynamics and trim calculations and gives the information to Overflow. The loose coupling allows for a modular approach and communication through input/output. The coupling methodology has been implemented following the approach of Potsdam *et al.*[13]

The numerical approach and the coupling process are described below.

2.1 Overset Grid Generation

The overset grid generation process using CGT can be divided into the following steps: geometry processing, surface grid generation, volume grid generation, and domain connectivity.[11]

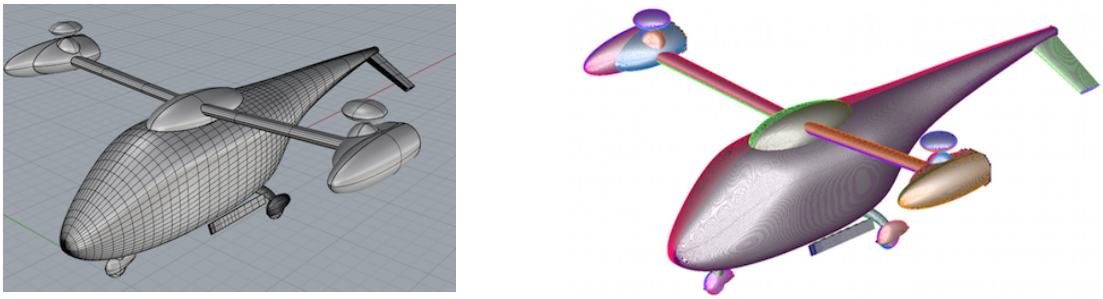

(a) CAD geometry.

(b) EGADS surface grid.

Figure 5: The side-by-side fuselage. The image on the left shows the CAD geometry, the image on the right shows the structured untrimmed patches obtained from the CAD geometry using EGADS. The patches are used as reference surfaces to generate the overset surface grids.

The geometry is usually obtained from a Computer Aided Design (CAD) model. Figure 5a shows the CAD model of the side-by-side vehicle. The Boundary Representation (BRep) is an object that holds both the topological entities and the geometric components.[14] In this work, a pre-processing step converts the analytical BRep solid from a STEP or IGES file into discrete representations for the BRep faces and edges. Access to the model topology and entities is accomplished through EGADS (the Engineering Geometry Aerospace Design System) API which is a foundational component of the Engineering Sketch Pad.[14] With the *egads2srf* tool, discrete representations are generated from each solid. Figure 5b shows the structured surface grid file for the SbS obtained using EGADS. This grid file contains an untrimmed structured patch for each face based on tessellation of the face parameter space. Another file obtained with *egads2srf* is a curve grid file containing tessellated edges. The curve grid file and the structured grid file from EGADS are used as an input for the overset surface grid generation step.

Overset structured surface meshes are typically created using a combination of algebraic and hyperbolic methods, depending on the number of initial curves on each surface domain. The generation of surface grids is the step that requires the most manual effort and expertise from the user.

With sufficient overlap between surface grids, the volume grids can be created easily with hyperbolic marching methods out to a fixed distance from the surface. Such methods provide orthogonal grids with tight clustering characteristics at the wall, which is essential for accurately capturing the boundary layer in viscous flow computations. The distance is chosen such that the outer boundaries of the NB volume grids are well clear off the boundary layer. The NB grids are then embedded inside OB Cartesian grids that extend to the far field.

Off-body Cartesian grids with uniform spacing surround the NB grids to resolve the wake region of interest. Coarser Cartesian grids efficiently expand the grid system to the far field, where each successive Cartesian grid is twice

DOI: 10.13009/EUCASS2019-359

as coarse as its previous neighbor. The far field boundary is 20 rotor radii away from the center of the vehicle in all directions. The resolved wake region has a uniform grid spacing of 10% of the tip chord length c_{tip}.

Surface grid resolution on the rotor blades is clustered in the chordwise direction near the airfoils leading and trailing edges to accurately resolve large pressure gradients. Subsequently, the spanwise resolution is clustered near the root and the tip. The normal grid spacing of all grids at the walls maintains $y^+ \leq 1$.

By using a trimmed approach, the domain connectivity step is robust and highly automated. In this study, the X-ray hole cutting method is used. An X-ray object is created for every component in the geometry (i.e. the blades, the hubs, the fuselage, the wings, etc.). The user has to supply the list of meshes that each X-ray object is allowed to cut, and an offset distance with which to grow each hole away from the body. Hole cutting is required between components and with the OB Cartesian grids. The hole cutting process is performed at each time step within the flow solver, allowing for the rotation of the blades relative to the fixed components.

2.2 High-Order Accurate Navier-Stokes Solver

Overflow solves the Navier-Stokes equations using finite differences with a variety of numerical algorithms and turbulence models. The time dependent, Reynolds-averaged Navier-Stokes (RANS) equations are solved in strong conservation form.

$$\frac{\partial \vec{q}}{\partial t} + \frac{\partial(\vec{F} - \vec{F_v})}{\partial x} + \frac{\partial(\vec{G} - \vec{G_v})}{\partial y} + \frac{\partial(\vec{H} - \vec{H_v})}{\partial z} = 0 \tag{1}$$

where $\vec{q} = [\rho, \rho u, \rho v, \rho w, e]^T$ is the vector of conserved variables; $\vec{F}$, $\vec{G}$ and $\vec{H}$ are the inviscid flux vectors; and $\vec{F_v}$, $\vec{G_v}$ and $\vec{H_v}$ are the viscous flux vectors.

In this study, the diagonal central difference algorithm is used with the 5^{th}-order accurate spatial differencing option with scalar dissipation. The physical time step corresponds to 0.25 degree rotor rotation, together with up to 50 dual-time sub-iterations, to improve time-accuracy by reducing the linearization errors. The numerical approach and time step were previously validated for various rotor flows.[15–17]

2.3 Hybrid Turbulence Modeling

The Overflow code has a choice of algebraic, one-equation, and two-equation turbulence models, including hybrid Reynolds-Averaged Navier-Stokes / Large Eddy Simulation (RANS/LES) models that close the RANS equations. In this study, the one equation Spalart-Allmaras[18] turbulence model is used primarily within the boundary layer.

The intent of the Detached Eddy Simulation (DES) model[18] is to be in RANS mode throughout the boundary layer, where the turbulent scales can be very small and need to be modeled, and in LES mode outside the boundary layer where the largest turbulent scales are grid-resolved. In this way, DES is a RANS/LES hybrid approach that mitigates the problem of artificially large eddy viscosity. The turbulence length scale d is replaced by $\overline{d}$, where $\overline{d}$ is the minimum of the distance from the wall, d, and the local grid spacing times a coefficient.

The DES approach assumes that the wall-parallel grid spacing $\Delta_{\|}$ exceeds the thickness of the boundary layer δ so that the RANS model remains active near solid surfaces. If the wall-parallel grid spacing is smaller than the boundary layer thickness, $\Delta_{\|} < \delta$, then the DES Reynolds stresses can become under-resolved within the boundary layer; this may lead to non-physical results, including grid-induced separation. Using Delayed Detached Eddy Simulation (DDES),[19] the RANS mode is prolonged and is fully active within the boundary layer. The wall-parallel grid spacing used in this study does not violate the hybrid-LES validity condition; thus DES and DDES should give similar results. Nevertheless, all computations have been performed using the DDES model for both NB and OB grids.

2.4 Comprehensive Analysis

Structural dynamics and rotor trim for the coupled calculations are performed using the comprehensive rotorcraft analysis code CAMRAD II.[12] CAMRAD II is an aeromechanics analysis of rotorcraft that incorporates a combination of advanced technologies, including multibody dynamics, nonlinear finite elements, and rotorcraft aerodynamics. The trim task finds the equilibrium solution for a steady state operating condition, and produces the solution for performance, loads, and vibration. The aerodynamic model for the rotor blade is based on lifting-line theory, using two-dimensional airfoil characteristics and a vortex wake model. CAMRAD II has undergone extensive correlation with performance and loads measurements on rotorcraft.

DOI: 10.13009/EUCASS2019-359

2.5 Loose Coupling Overflow – CAMRAD II

A loose coupling approach between Overflow and CAMRAD II based on a trimmed periodic rotor solution is implemented. The comprehensive code provides the trim solution and blade motions. The high-fidelity CFD calculates the airloads. Figure 6 shows the flow diagram of the loose coupling strategy. In summary, the CFD airloads replace the comprehensive airloads while using lifting line aerodynamics to trim and computational structural dynamics to account for blade deformations. In this work, the SbS blades have flap hinges, but are considered rigid, and consequently there will not be elastic motions in the blades. The comprehensive analysis is still needed to get the trim angles and rigid blade motions for the CFD.

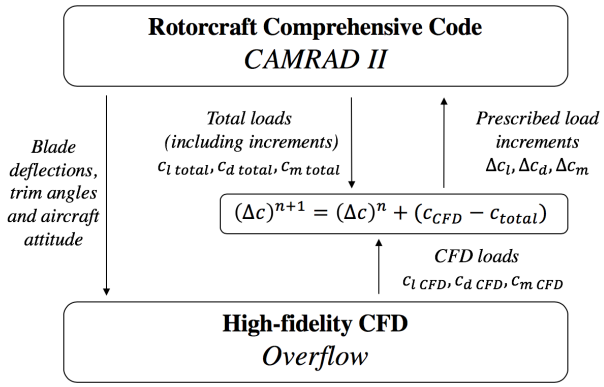

Figure 6: Flow diagram for CFD/Comprehensive Analysis loose coupling methodology.

The iterative loose coupling process is summarized next. The simulation is initialized with a comprehensive analysis resulting in a trimmed rotor solution obtained with lifting line aerodynamics. This analysis creates initial quarter chord motions as a function of the radius r and the azimuth ψ, for each rotor. In addition, the aircraft attitude is also obtained from CAMRAD II. The motions and aircraft pitch angle are given to the CFD. The CFD analysis accounts for the entire flow field, and therefore it only requires the structural motion. The CFD is run with the prescribed motions and angles, for two to three full rotor revolutions for the first coupling step. Overflow outputs the normal force N', pitching moment M', and chord force C' as a function of radius and azimuth.

Then, the aerodynamic force and moment coefficients increments (Δc) that are used in the comprehensive code at the next iteration $n+1$ are calculated. The increments are the difference between the CFD loads and the comprehensive lifting line solution required to trim from the previous step n, plus the load increments from the previous step:

$$(\Delta c)^{n+1} = (\Delta c)^n + (c_{CFD} - c_{total}) \tag{2}$$

For the initial step, the increments are the difference between CFD and the total loads from the 0^{th} run in CAMRAD II:

$$(\Delta c)^1 = (c_{CFD} - c_{total})$$

The sectional pitching moment $M^2 c_m$, normal force $M^2 c_n$ and chord force $M^2 c_c$ coefficients are defined as:

$$M^2 c_m = \frac{M'}{\frac{1}{2}\rho a^2 c^2} \tag{3}$$

$$M^2 c_n = \frac{N'}{\frac{1}{2}\rho a^2 c} \tag{4}$$

$$M^2 c_c = \frac{C'}{\frac{1}{2}\rho a^2 c} \tag{5}$$

With the new quarter chord motions of the retrimmed rotor and the new aircraft attitude, the CFD is rerun. The previous CFD flow solution is used as restart condition. The coupling is performed every half or quarter rotor revolution. The coupling solution is considered to be converged when collective and cyclic control angles and the CFD aerodynamic forces do not change between iterations. The CFD flow solution is usually converged after 10 to 20 rotor revolutions.

DOI: 10.13009/EUCASS2019-359

The coupling procedure is valid as long as the rotor loads are periodic. This approach is still good if there is some aperiodicity in the vortex wake, which is often the case in high-resolution turbulent simulations.

The coupled Overflow – CAMRAD II simulations are completely automatized using a Python code and Fortran post-processing functions. All simulations were run on NASA's supercomputers Pleiades and Electra, using from 1000 to 2500 cores.

3. Results

In this section, the results obtained for the three vehicles shown in the Introduction are presented: the DJI Phantom 3 in hover, the SUI Endurance in forward flight, and the side-by-side air taxi in cruise.

The Overflow Navier-Stokes CFD code and the Chimera Grid Tools software are used throughout this study. All computations have been carried out with NASA's supercomputers Pleiades and Electra located at the NASA Advanced Supercomputing (NAS) facilities at NASA Ames Research Center.

Each vehicle will be presented in a similar way: the overset grids that model the geometry are introduced first, then the CFD results from Overflow for different configurations will be shown. The effects of the changes in arrangements will be compared, extracting conclusions regarding good practice in the design of multi-rotor VTOL vehicles. For the side-by-side vehicle, the blade motions and aircraft attitude are obtained using CAMRAD II following the loose coupling methodology depicted in the previous section 2.5.

3.1 The DJI Phantom 3 in Hover

The quadcopter DJI Phantom 3 is constructed by incorporating the four rotors to the X-shaped airframe in diagonal-opposed clock-wise (CW) and counter-clock-wise (CCW) positions for torque cancellation.

3.1.1 Overset Grids

The geometries for a simplified airframe and the DJI CF blades have been modeled. The overset grids are generated using CGT following the procedure summarized in section 2.1. For a more complete guide on how to generate high-quality overset grids and the good practices, see Chan *et al.*[11]

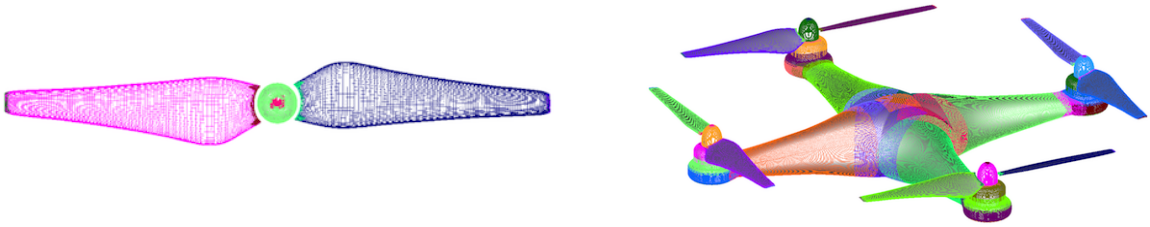

(a) Overset surface grids for Floureon's CF replica blades.

(b) Overset surface grids for the simplified DJI Phantom.

Figure 7: Overset grids of the DJI Phantom simplified airframe.

The simplified airframe has been modeled using high-order polynomials and CAD software. Collar grids are used at the junctions, and cap grids cover singular axis. The CF rotor blades were obtained at NASA Ames using high resolution laser scan techniques. The rotor blades are defined by airfoil profiles at different radii from the point cloud. The profiles are connected and smoothed, obtaining the whole blade. Each rotor system consists of two blades attached to a central hub. O-grids are used for the blades. Cap grids are needed at the blade tips and the axis of the hub. At the junction with the hub, collar grids are used. Figure 7 shows the overset surface grids of the blades and the airframe.

The NB volume grids for the simplified airframe consist of 86 overset grids, with a total of NB and OB 387 million grid points.

3.1.2 Effect of Rotor Mounting in Hover

The rotational speed in hover for the DJI Phantom 3 was measured in flight test and it is equal to $\Omega_{hover} = 5400$ RPM. In this section, the simplified airframe is simulated with the CF blades for three rotor-mounting options:

- Overmount, the conventional configuration.

DOI: 10.13009/EUCASS2019-359

- Undermount, the rotors are placed on the underside of the fuselage arms instead of above. The separation between the rotors and the arms below is the same than with the overmount rotors.
- Off-body undermount. The rotors are at a distance of $0.25R$ below the hub.

With Overflow, simulations are run for the equivalent of 21 rotor revolutions, reaching convergence of 3.0 orders of magnitude drop in sub-iteration residual, for a quasi-periodic solution. For Ω_{hover}, the tip Mach number is $M_{tip} = 0.2$, and the Reynolds number is $Re = 37300$.

A more detailed study can be found in previous work by the authors.[6] Here the most impactful results are summarized.

Figure 8 shows a comparison of velocity magnitude and the pressure coefficients, on a vertical plane through the center of the vehicle. Of the three configurations, the overmount configuration exhibits the highest speed downwash from the inboard rotor blades, whereas the off-body undermount configuration exhibits the lowest. While the high pressure below the overmount rotors *pushes down* the fuselage, the low pressure above the undermount rotors *pulls down* the fuselage by almost the same force as the overmount configuration. Compared to the undermount configuration, the fuselage of the off-body undermount configuration experiences much less download. However, without significant interference from the fuselage, the four rotors experience strong interactions among themselves.

Pressure fluctuations on the surface of the vehicle and near it can be observed for the overmount and undermount configurations, being much stronger in the undermount case. For the off-body undermount these fluctuations are weak.

Table 1 shows that the undermount configuration generates 1% less total thrust than the overmount, and the off-body undermount configuration generates 2% less than the undermount configuration. The thrust only from rotors for the off-body undermount is 6% less than the undermount and 7% less than the overmount.

3.1.3 The Octorotor

In order to study the effect of coaxial rotors on the performance of a quadcopter, the configuration has been modified by the addition of four rotors beneath the fuselage. The resulting vehicle configuration employs eight rotors and the simplified airframe. The lower rotors rotate in opposite direction than the upper rotors, that is the rotors are counter-rotating, common practice in coaxial helicopters for torque cancellation. The total number of NB and OB grid points for the vehicle system is 250 million.

Figures 8 (g) and (h) show the velocity magnitude and the pressure for the torque-balanced octorotor.[7] Note stronger pressure fluctuations on the surface of the vehicle and nearby, than in the quadcopter configurations seen in the previous section.

Rotor positions are in phase. Mounting rotors both above and below arms can increase the thrust significantly, but by losing up to 41% efficiency[1]. Yoon et al.[7] showed that the torque-balanced vehicle generates 82% more thrust than the quadcopter, see table 1.

	$C_{T,rot}$	$C_{T,fus}$	$C_{T,tot}$
Overmount	1.025	-0.076	0.949
Undermount	1.016	-0.080	0.936
OB Undermount	0.954	-0.038	0.916
Octorotor Coaxial	1.883	-0.154	1.729

Table 1: Rotor thrust $C_{T,rot}$, fuselage download $C_{T,fus}$, and total thrust $C_{T,tot}$, for various quadrotor configurations (Forces have been normalized by $4x$ the CF isolated single rotor thrust).

3.2 SUI Endurance

The second vehicle presented in this work is the SUI Endurance. The SUI quadcopter's original geometry has been slightly modified for the aerodynamic simulations, by removing, for example, the interior parts or the small pieces used to fold the arms, which do not change the main flow. The aerodynamic SUI configuration consists of the fuselage, four rotors, four arms, four motors, camera mounting, and landing gear. Again, the rotors are added so that there are two diagonally opposed rotors that rotate CW and the other two diagonally opposed rotors rotate CCW. The rest of the vehicle (fuselage, four arms, four motors, and landing gear) has been represented using a CAD model of the SUI quadcopter, provided by SUI to NASA Ames.

[1]The interference-induced power in coaxial rotors is $\sqrt{2}$, which is a 41% increase in induced power relative to the power required to operate the two rotors in complete isolation.

DOI: 10.13009/EUCASS2019-359

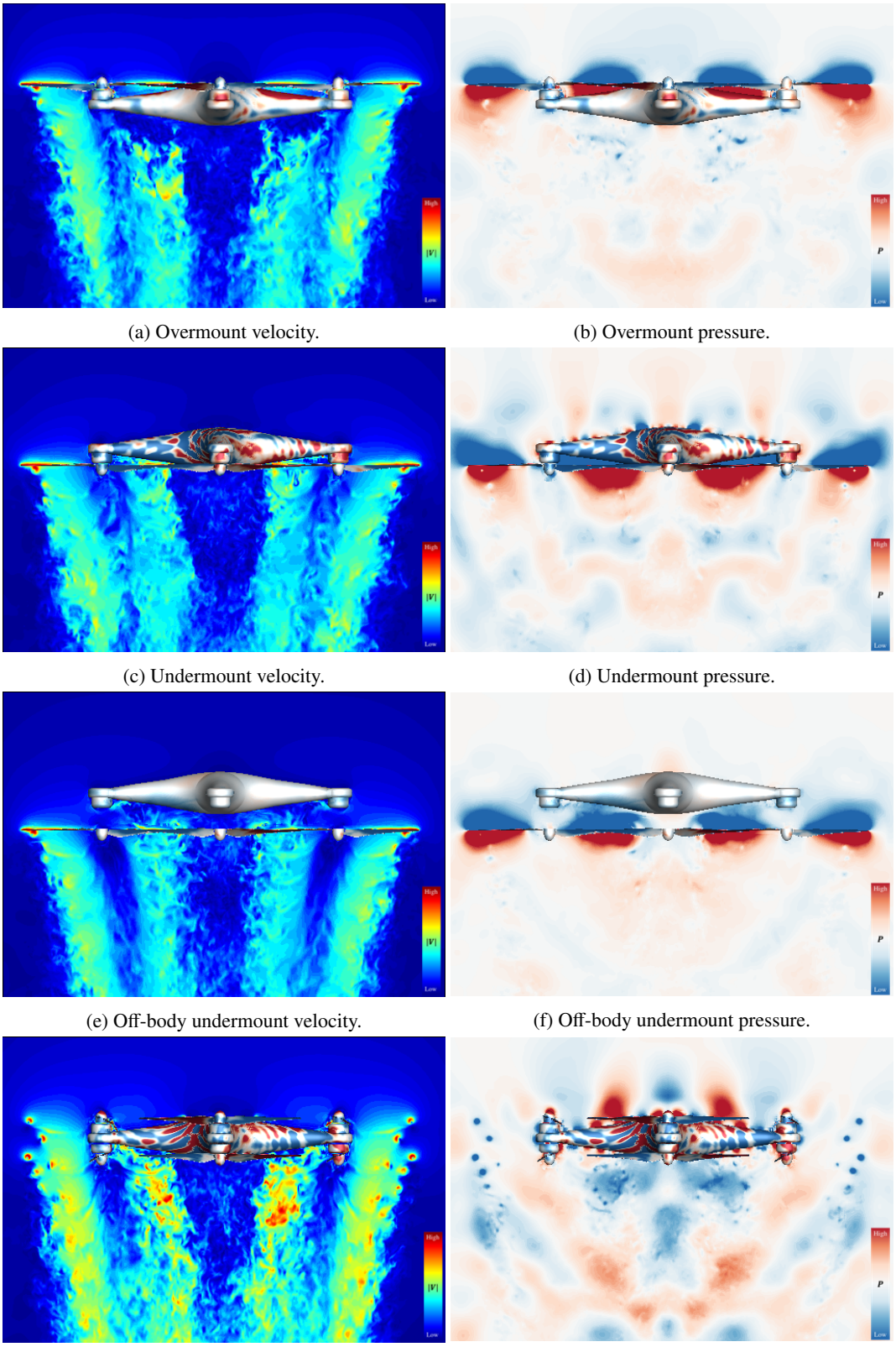

(a) Overmount velocity.

(b) Overmount pressure.

(c) Undermount velocity.

(d) Undermount pressure.

(e) Off-body undermount velocity.

(f) Off-body undermount pressure.

(g) Octorotor velocity.

(h) Octorotor pressure.

Figure 8: Velocity magnitude and pressure for overmount (a and b), undermount (c and d), off-body undermount (e and f), and octorotor (g and h). Pressure shown at the surface.

DOI: 10.13009/EUCASS2019-359

3.2.1 Overset Grids

The quadcopter is constructed by adding to the fuselage two fore arms and two aft arms, each arm supporting at its end the motor and the rotor blades. The fore and aft arms form an angle of 60 and 30 degrees with the fuselage longitudinal axis, respectively. The left fore blades, left aft blades, right aft blades, and right fore blades (pilot view) rotate CW, CCW, CW and CCW, respectively. The landing gear is also added to the fuselage.

There are 41 million NB grid points with 176 grids, and 541 million NB and OB grid points. Figure 9b shows the top view of the surface grids of the SUI quadcopter, with the names of the components.

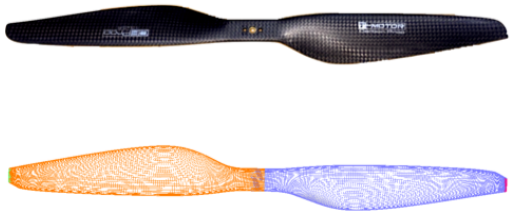

(a) T-Motor P15x5 CF blades for the SUI Endurance. The top image shows a picture, the bottom image shows overset surface grids top view.

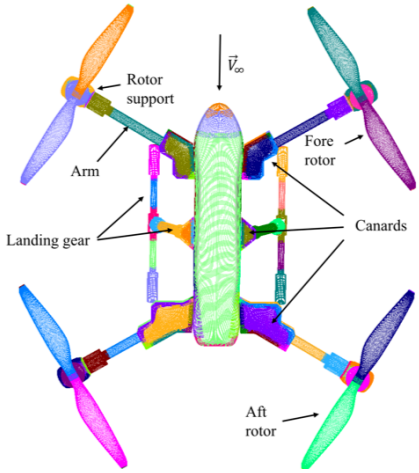

(b) SUI Endurance overset surface grids top view, with the components.

Figure 9: Overset surface grids for the SUI Endurance quadcopter.

The rotor blades mounted on the SUI Endurance are the original T-Motor P15x5 CF blades; see figure 9a. The geometry information was obtained by using high-resolution laser scanning conducted at NASA Ames. Airfoil profiles at different radii were generated from the point cloud, and the profiles were connected and smoothed, obtaining the whole blade. At the center, the blades were joined together without a hub. O-grids are used for the blades, and cap grids are generated for the blade tips.

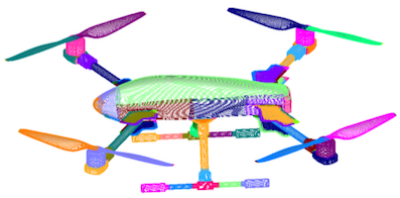

(a) Standard SUI.

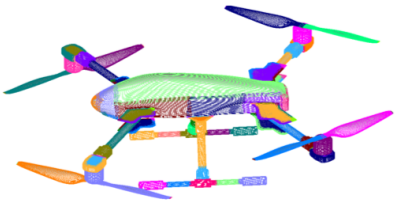

(b) Hybrid SUI.

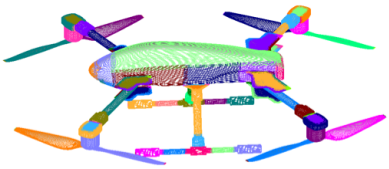

(c) Undermount SUI.

Figure 10: Overset surface grids for different rotor mountings in the SUI Endurance.

In order to study the effect of rotor mounting in forward flight, three configurations of the SUI Endurance geometry have been modeled:

- Standard SUI, the conventional SUI Endurance configuration with the four rotors overmounted; see Figure 10a.
- Hybrid SUI, the fore rotors are undermounted and the aft rotors remain overmounted; see Figure 10b.
- Undermount SUI, all rotors are undermounted; see Figure 10c.

DOI: 10.13009/EUCASS2019-359

3.2.2 Effect of Rotor Mounting in Forward Flight

The forward flight conditions simulated match the conditions of the flight tests conducted. The flow velocity is $V_\infty = 10\ m/s$, $\alpha = -7.7^o$. Trim conditions were measured for the SUI standard vehicle. Fore and aft rotors rotate at different rotational speeds for the quasi-steady forward flight condition, $\Omega_{fore} = 3510$ RPM and $\Omega_{aft} = 4410$ RPM. The advance ratio based on the fore rotors is $\mu = 0.142$.

Figure 11 (a) shows the velocity magnitude contours for the standard SUI vehicle. With the idea of increasing the thrust of the aft rotors, the authors decided to undermount the fore rotors and keep the aft rotors overmounted, to obtain what it has been called a *hybrid configuration*. With this new arrangement, the aft rotors are no longer immersed in the wake of the fore rotors; see figure 11 (b). As a consequence, the thrust from the aft rotors increases substantially. The fore rotors thrust decreases slightly as a result of undermounting them, as observed in the DJI sections. However, the increase in aft-rotor thrust is much more important than the decrease in the fore-rotor thrust[2]. We can conclude that the hybrid SUI is more efficient aerodynamically than the standard configuration.

Finally, one last SUI vehicle has been simulated, the undermount SUI, see figure 11 (c). The download from the arms is important for overmounted rotors, and the objective of the undermount SUI is to reduce this effect.

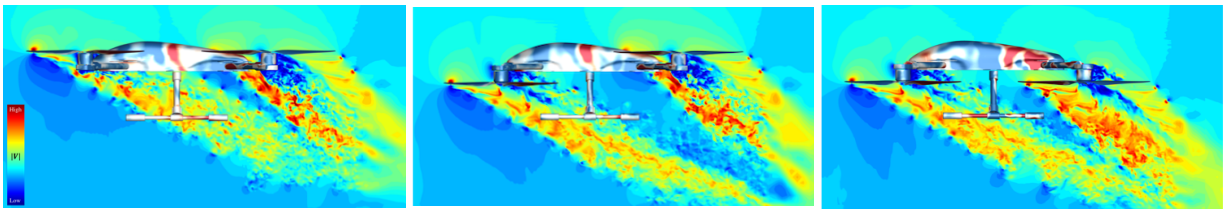

(a) Standard SUI. (b) Hybrid SUI. (c) Undermount SUI.

Figure 11: SUI quadcopter in forward flight. Figure (a) shows the standard SUI, (b) shows the hybrid SUI, and (c) shows the undermount SUI. Note the interactions rotor-rotor for the standard and undermount configurations. Pressure shown at the surface.

Table 2 shows the performance of each component. The thrust/lift coefficient is decomposed into its horizontal part, c_x, and its vertical part c_y, for each component of the vehicle, as it can be seen in figure 12. The final values displayed have been normalized by 4x the thrust of the isolated rotor in hover.

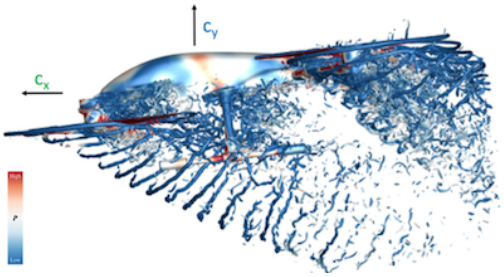

Figure 12: Hybrid SUI quadcopter in forward flight. Schematic of the force coefficients acting on the quadcopter, c_x and c_y.

First, when comparing the horizontal forces c_x, where negative values indicate drag, one can observe the increase in performance of the fore rotors in the hybrid case. Interactions with the aft rotors are minimal, and it seems that undermounting the rotors is beneficial in the SUI configuration, as the aft rotors undermounted are slightly better than in the standard case. The drag of the fuselage and landing gear is similar in all cases, smoothly increasing from the standard case to the undermount case. In the case of the canards, this effect is more noticeable. The standard SUI canards contribute positively to the forward force, but when the rotors are undermounted canards switch sign and contribute to the drag. One of the main actors in horizontal forces are the arms. Placing the rotors underneath decreases the drag of the arms substantially. Adding all components makes the hybrid the best configuration for forward flight, with an improvement of 63% in c_x.

In the case of the vertical forces c_y, the fore rotors are better when they are overmounted, as seen in the DJI cases. The aft rotors perform the best in the hybrid case, thanks to the reduction of interactions with the fore rotors. The fuselage generates some vertical force, contributing the most in the standard case, probably due to the low pressure regions below the rotors near the fuselage. This effect is lowered when the rotors are undermounted. The effect of the landing gear is not very important. The canards provide significant vertical force in the standard configuration. Again as with the fuselage, their contribution to vertical force is diminished when the rotors are placed underneath the arms. Download from the arms is similar between the standard and the hybrid cases. Fully undermounting the rotors reduces

[2]New trim conditions would need to be found for the modified configurations. Because the thrust of the rotors changes, the rotational speed should be adjusted accordingly in order to keep the same quasi-steady forward flight condition. Still, the aft rotors are more efficient because they are no longer in the wake of the fore rotors.

DOI: 10.13009/EUCASS2019-359

	c_x Standard	c_x Hybrid	c_x Undermount	c_y Standard	c_y Hybrid	c_y Undermount
Fore rotors	0.053	0.056	0.055	0.633	0.631	0.629
Aft rotors	0.075	0.079	0.080	0.836	0.885	0.828
Fuselage	-0.003	-0.004	-0.005	0.042	0.022	0.015
Landing gear	-0.015	-0.019	-0.020	0.002	0.002	0.002
Canards	0.003	-0.002	-0.008	0.051	0.014	0.011
Arms	-0.091	-0.075	-0.070	-0.046	-0.049	-0.027
TOTAL	0.022	0.036	0.033	1.517	1.504	1.436

Table 2: SUI Endurance quadcopter horizontal force coefficient c_x and vertical force coefficient c_y in forward flight. Forces $F_{x,i}$ and $F_{y,i}$ have been normalized by $\rho(\Omega_{fore}R)^2A$ and then by 4x the thrust of the isolated SUI rotor in hover.

the download force. In total, the standard case has the highest lift but very close to the hybrid SUI, with just a difference of 1%.

Overall, the performance of the hybrid SUI is better than the two other configurations. A hybrid quadcopter is more efficient aerodynamically in forward flight than a fully overmount or undermount quadcopter.

3.3 Side-by-side Air Taxi

The comprehensive rotorcraft code CAMRAD II and the high-fidelity CFD code Overflow are used throughout this study to simulate the side-by-side urban air taxi in edgewise forward flight.

3.3.1 Overset Grids

Figure 13 shows the surface grids for the SbS vehicle with the rotors. For this study, the landing gear and the strakes have been omitted. The grid system consists of the main fuselage, the wing, the engines, the tail, the rotors, and the rotor hubs.

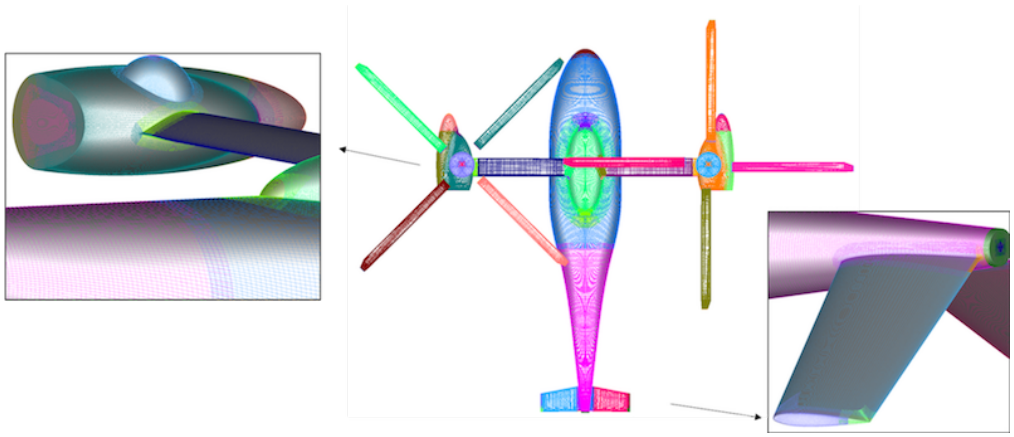

Figure 13: Side-by-side overset surface grids, top view. On the left, the attachment of the engine with the wing is shown in detail. The image on the right shows the attachment of the tail to the fuselage.

The airframe grids have been generated using the CAD model shown in Figure 5a as reference. The profiles used to build the blade are the VR12 airfoils from $r = 0$ to $r = 0.85R$, and the SSCA09 airfoils from $r = 0.95R$ to the tip, $r = R$. The transition between the two different airfoil sections is smooth (linear interpolation with the radial stations). The blade is tapered and swept near the tip. Figure 14 shows in detail the SbS blade.

The multi-rotor system consists of two overlapping rotors, each rotor made up of four blades. The right rotor rotates counter-clockwise (CCW), and the left rotor rotates clockwise (CW), therefore the advancing blade is always outboard. The overlapping distance can be changed and its effect on the airloads, performance, and wake geometry in cruise will be the main subject of study in the present work.

The rotor system consists of 30 NB grids with 25 NB million grid points, and 235 to 260 million total (NB + OB) grid points, depending on the overlapping distance. For the complete vehicle, there is a total of 74 NB grids with 40 NB million grid points, the total number of NB and OB grid points is 300 million.

DOI: 10.13009/EUCASS2019-359

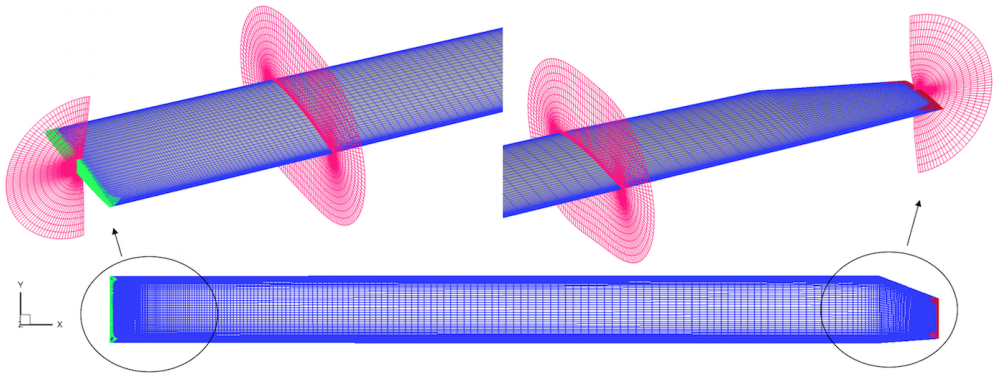

Figure 14: Blade overset grids for the side-by-side urban air taxi. The NB root and tip grids are shown in detail. Cap grids are used for the root (green) and tip (maroon), O-grids are used for the blade (blue). Slices of the volume grids are shown in magenta. There is clustering near the leading edge, trailing edge, blade tip and blade root, in order to solve the large pressure gradients near these regions.

3.3.2 Effect of Rotor Overlap in Cruise

The side-by-side rotors without airframe are simulated in forward flight using the Overflow - CAMRAD II loosely coupled strategy described in the Numerical Approach section. Five different wing spans are considered in this work: $0.75D$ (25% overlap), $0.85D$ (15% overlap), $0.95D$ (5% overlap), $1D$ (0% overlap) and $3D$ spans (isolated rotors). The $3D$ span case is representative of *isolated* side-by-side rotors. Yoon et al.[17] showed that the normalized vertical force coefficient of rotors with an inter-rotor separation of $2D$ (wing span = $3D$) is 99.9% that of the isolated single rotor in hover conditions. Therefore, the $3D$ span case represents the isolated rotor case.

The flight condition simulated is the best-range cruise, at 5000 ft ISA +20^{o}C, with an advance ratio of $\mu = 0.356$.

The vortex wakes for 25%, 15%, 5% and 0% overlap distances are shown in Figures 15a, 15b, 15c, and 15d, respectively. The vortex wake of the side-by-side isolated rotors is shown in Figure 15e. Finally, the vortex wake of the side-by-side complete vehicle with 15% overlapped rotors is shown in Figure 15f. The vortices are visualized by using iso-surfaces of the Q-criterion vorticity, and they are colored with the vorticity magnitude. All figures use the same values of Q-criterion and vorticity magnitude.

Some common flow features that appear in the vortex wakes of the four cases with overlap (25%, 15%, 5% and 0%[3]), the side-by-side isolated rotors and the complete vehicle, are: blade-vortex interactions, blade tip-vortex rollup downstream at the exterior (advancing side) of both rotors, interaction in the overlap region (retreating side) of one vortex wake with another, development of worm-like vortical structures[20] in the downstream wake, and separated wake flow from the hubs.

L/D_e	25% overlap	15% overlap	15% full vehicle	5% overlap	0% overlap	Isolated
CAMRAD II free wake	9.43	10.05	10.05	9.76	9.60	8.94
Overflow-CAMRAD II	7.72	8.15	8.67	8.12	8.02	7.20

Table 3: Side-by-side performance calculations of the rotor system (right rotor + left rotor) for rotors only and for the complete vehicle. The rotor efficiency in cruise, $L/D_e = WV/(P_i + P_0)$, is shown.

The calculated performance for each overlap are shown in Table 3. The trend obtained from the comprehensive analysis is confirmed here with the high-fidelity CFD results: the rotors with 15% overlap are the most efficient in cruise. That is, side-by-side rotors with 15% overlap are about 15% better than two side-by-side isolated rotors. The table also shows the comparison of the cruise performance of the side-by-side vehicle (rotors + airframe) with the side-by-side rotors. The vehicle increases the rotor efficiency by 6%.

4. Summary

High-order accurate Computational Fluid Dynamics simulations have been carried out for several multi-rotor vehicles. NASA's supercomputers Pleiades and Electra were essential for this work as the overset grids have hundred of millions

[3]Even with 0% overlap there are rotor-rotor interactions, as it has been observed throughout this study. In fact, the separation needed for removing rotor-rotor interactions, is of two rotor diameters ($2D$), thus the rotors rotational centers are separated by $3D$, as demonstrated by Yoon et al.[17]

DOI: 10.13009/EUCASS2019-359

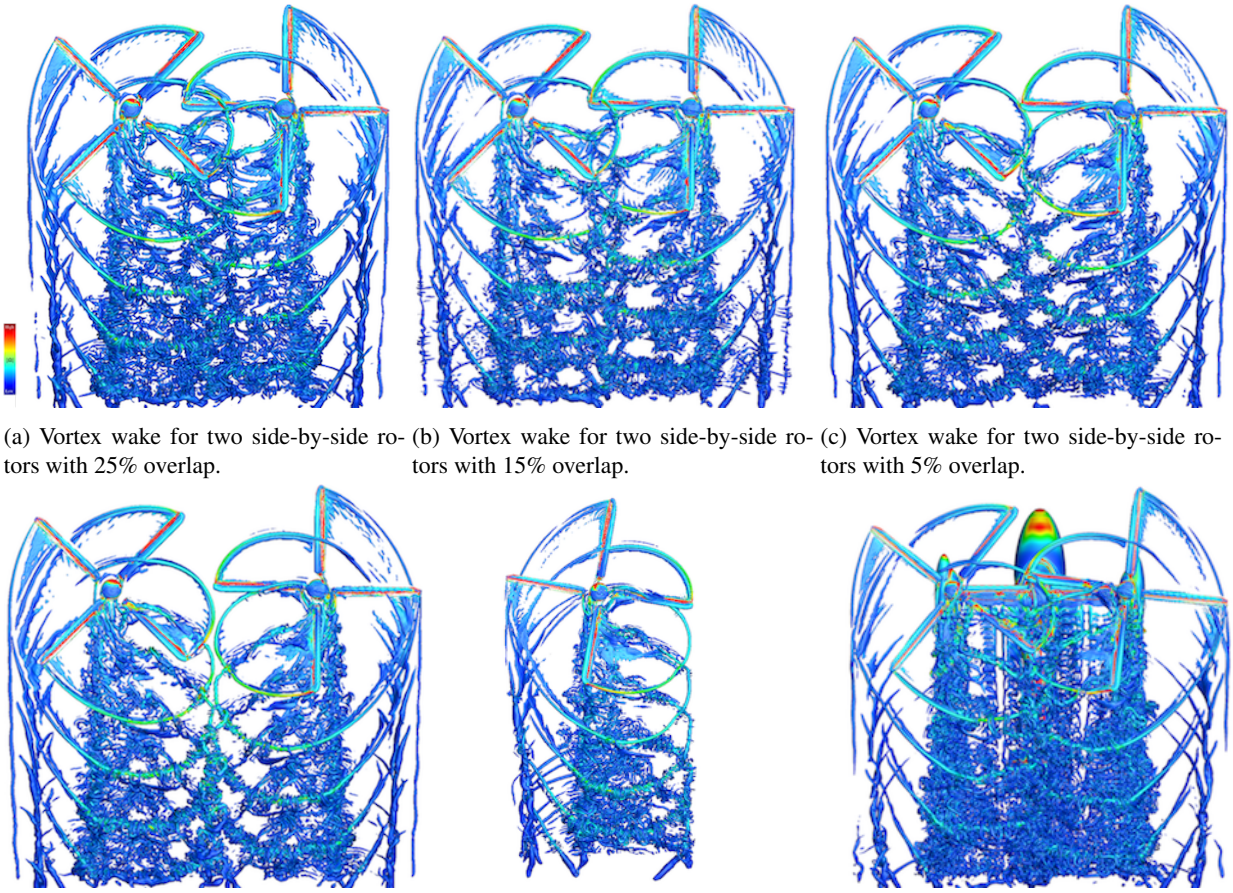

(a) Vortex wake for two side-by-side rotors with 25% overlap.

(b) Vortex wake for two side-by-side rotors with 15% overlap.

(c) Vortex wake for two side-by-side rotors with 5% overlap.

(d) Vortex wake for two side-by-side rotors with 0% overlap.

(e) Vortex wake for two side-by-side isolated rotors (showing only left rotor).

(f) Vortex wake of side-by-side complete vehicle with 15% overlap.

Figure 15: Q-criterion vorticity iso-surfaces for side-by-side rotors only (a through e) and complete vehicle (f) in cruise.

of grid points.

First, a complete study of the DJI Phantom 3 and its variants in hover has been carried out. The effects of over- and under-mounting the rotors have been studied, concluding that under-mounting the rotors reduces the thrust and produces stronger pressure fluctuations. An octorotor increases the thrust but also the power required to fly it.

The SUI Endurance simulations in forward flight have thrown insight on better designs during cruise: under-mounting the fore rotors and over-mounting the aft rotors improves the aerodynamic efficiency of the vehicle, by reducing the interactions between the fore and aft rotors. The so called *hybrid SUI* increases the forward horizontal force by 63% compared to the standard SUI.

The effects of the rotor overlap distance of NASA's side-by-side urban air taxi concept have been analyzed. A loose coupled approach to simulate the flow of the twin rotor system in cruise conditions has been followed. The rotorcraft comprehensive code CAMRAD II and the overset Navier-Stokes CFD solver Overflow have been coupled. The performances of the rotors have been presented, showing that overlapping rotors are more efficient in cruise than two isolated rotors, and the best configuration is for 15% rotor overlap.

The concept vehicles are intended to focus and guide NASA research activities in support of aircraft development for emerging aviation markets, in particular vertical take-off and landing air taxi operations.

5. Acknowledgements

This work was supported by the Revolutionary Vertical Lift Technology and the DELIVER projects. The computations utilized the Electra supercomputer at NASA Advanced Supercomputing Division. The authors would like to thank Wayne Johnson, Jasim Ahmad, Brian Allan, Gloria Yamauchi, Chris Silva, and Eduardo Solis for helpful discussions.

DOI: 10.13009/EUCASS2019-359

References

[1] Ventura Diaz, P., Johnson, W., Ahmad, J., and Yoon, S., "The Side-by-side Urban Air Taxi Concept", AIAA Paper 2019-2828, The AIAA Aviation Forum 2019, Dallas, Texas, June 2019.

[2] Johnson, W., *Helicopter Theory*, Dover Publications, 1994.

[3] Ventura Diaz, P., and Yoon, S., "High-Fidelity Computational Aerodynamics of Multi-Rotor Unmanned Aerial Vehicles", AIAA Paper 2018-1266, The AIAA SciTech Forum 2018, Kissimmee, Florida, January 2018.

[4] Ventura Diaz, P., Caracuel Rubio, R., and Yoon, S., "Simulations of Ducted and Coaxial Rotors for Air Taxi Operations", AIAA Paper 2019-2825, The AIAA Aviation Forum 2019, Dallas, Texas, June 2019.

[5] Ventura Diaz, P., and Yoon, S., "A Physics-Based Approach to Urban Air Mobility", The European Rotorcraft Forum, Paper 18, Delft, The Netherlands, September 2018.

[6] Yoon, S., Ventura Diaz, P., Boyd, D. D., Chan, W. M., and Theodore, C. R.,"Computational Aerodynamic Modeling of Small Quadcopter Vehicles", AHS Paper 73-2017-0015, The 73rd Annual AHS International Forum & Technology Display, Fort Worth, Texas, May 2017.

[7] Yoon, S., Chan, W. M., and Pulliam, T. H., "Computations of Torque-Balanced Coaxial Rotor Flow", AIAA Paper 2017-0052, The 55th AIAA Aerospace Sciences Meeting, Grapevine, Texas, January 2017.

[8] Johnson, W., Silva, C., and Solis, E., "Concept Vehicles for VTOL Air Taxi Operations", The AHS International Technical Meeting on Aeromechanics Design for the Transformative Flight, San Francisco, California, January 2018.

[9] Johnson, W., and Silva, C., "Observations from Exploration of VTOL Urban Air Mobility Designs", The Asian/Austrialian Rotorcraft Forum, Jeju Island, Korea, October 2018.

[10] Pulliam, T. H., "High Order Accurate Finite-Difference Methods: as seen in OVERFLOW", AIAA Paper 2011-3851, June 2011.

[11] Chan, W. M., Gomez, R. J., Rogers, S. E., Buning, P. G., "Best Practices in Overset Grid Generation", AIAA Paper 2002-3191, The 32nd AIAA Fluid Dynamics Conference, St. Louis, Missouri, June 2002.

[12] Johnson, W., "Rotorcraft Aerodynamic Models for a Comprehensive Analysis", American Helicopter Society 54th Annual Forum, Washington, D. C., May 1998.

[13] Potsdam, M., Yeo, H., and Johnson, W., "Rotor Airloads Prediction Using Loose Aerodynamics/Structural Coupling", American Helicopter Society 60th Forum, Baltimore, Maryland, June 2004.

[14] Haimes, R., and Dannenhoffer, J. F., "The Engineering Sketch Pad: A Solid-Modeling, Feature-Based, Web-Enabled System for Building Parametric Geometry", AIAA Paper 2013-3073, The 21st AIAA Computational Fluid Dynamics Conference, San Diego, California, June 2013.

[15] Yoon, S., Chaderjian, N. M., Pulliam, T. H., and Holst, T. L., "Effect of Turbulence Modeling on Hovering Rotor Flows", AIAA Paper 2015-2766, The 45th AIAA Fluid Dynamics Conference, Dallas, Texas, June 2015.

[16] Yoon, S. Lee, H. C., and Pulliam, T. H., "Computational Study of Flow Interactions in Coaxial Rotors", The AHS Technical Meeting on Aeromechanics Design for Vertical Lift, San Francisco, California, January 2016.

[17] Yoon, S., Lee, H. C., and Pulliam, T. H., "Computational Analysis of Multi-Rotor Flows", AIAA Paper 2016-0812, The 54th AIAA Aerospace Sciences Meeting, AIAA SciTech Forum, San Diego, California, January 2016.

[18] Spalart, P. R., Jou, W-H., Strelets, M., and Allmaras, S. R., "Comments on the Feasibility of LES for Wings and on a Hybrid RANS/LES Approach", Advances in DNS/LES, Greyden Press, 1997, pp. 137-147.

[19] Spalart, P. R., "Strategies for Turbulence Modeling and Simulations", International Journal of Heat and Fluid Flow, 21, 2000, pp. 252-263.

[20] Chaderjian, N., "Navier-Stokes Simulation of UH-60A Rotor/Wake Interaction Using Adaptive Mesh Refinement", American Helicopter Society 73rd Annual Forum, Fort Worth, Texas, May 2017.